BNL-108311-2015-JA

Journal of Materials Chemistry C

ARTICLE

# The role of interparticle heterogeneities in the selenization pathway of Cu-Zn-Sn-S nanoparticle thin films: A real-time study†

Received 00th January 20xx,
Accepted 00th January 20xx

DOI: 10.1039/x0xx00000x

www.rsc.org/

Nathaniel J. Carter,[a] Roland Mainz,[b] Bryce C. Walker,[a] Charles J. Hages,[a] Justus Just,[b] Manuela Klaus,[b] Sebastian S. Schmidt,[b] Alfons Weber,[b] Wei-Chang D. Yang,[c] Ole Zander,[b] Eric A. Stach,[d] Thomas Unold[b] and Rakesh Agrawal*[a]

Real-time energy dispersive x-ray diffraction (EDXRD) analysis has been utilized to observe the selenization of Cu-Zn-Sn-S nanoparticle films coated from three nanoparticle populations: Cu- and Sn-rich particles roughly 5 nm in size, Zn-rich nanoparticles ranging from 10 to 20 nm in diameter, and a mixture of both types of nanoparticles (roughly 1:1 by mass), which corresponds to a synthesis recipe yielding CZTSSe solar cells with reported total-area efficiencies as high as 7.9%. The EDXRD studies presented herein show that the formation of copper selenide intermediates during the selenization of mixed-particle films can be primarily attributed to the small, Cu- and Sn-rich particles. Moreover, the formation of these copper selenide phases represents the first stage of the CZTSSe grain growth mechanism. The large, Zn-rich particles subsequently contribute their composition to form micrometer-sized CZTSSe grains. These findings enable further development of a previously proposed selenization pathway to account for the roles of interparticle heterogeneities, which in turn provides a valuable guide for future optimization of processes to synthesize high quality CZTSSe absorber layers.

## Introduction

Thin film solar cells with $Cu_2ZnSn(S,Se)_4$ (CZTSSe) absorber layers offer significant promise as a sustainable and low-cost photovoltaic technology. Comprising earth abundant Cu, Zn, Sn, and S, CZTSSe is characterized with a direct band gap tunable between 1.0 and 1.5 eV depending on the relative content of S and Se in order to ideally match solar irradiance. Additionally, CZTSSe possesses a high absorption coefficient, thereby minimizing the amount of material necessary to absorb the incident solar radiation.[1,2] CZTSSe devices processed from hydrazine-based precursor solutions have reached power conversion efficiencies as high as 12.6%,[3] while vacuum-based deposition techniques have yielded efficiencies up to 11.6%.[4–6] CZTSSe devices fabricated from nanoparticle inks formulated using relatively benign solvents have achieved total-area efficiencies of 9.0%;[7] this value increases to 9.4% when Ge is partially substituted for Sn to create the alloy CZTGeSSe in order to increase the absorber band gap.[8] In both cases, the formation of the dense CZT(Ge)SSe absorber from CZT(Ge)S sulfide nanoparticles by heating in the presence of Se vapor (selenization) represents a crucial step in the device fabrication process due to the improved transport properties associated with larger grains and denser films.[8–12] Directed improvements in device performance necessary for commercialization of this promising technology require elucidation of the insufficiently understood selenization mechanism.

Previous research investigated the selenization mechanism in films of CZTS nanoparticles via real-time energy-dispersive x-ray diffraction (EDXRD) and identified the growth mechanism through the various phases that grow and recede throughout the process;[13] in this work, it was hypothesized that the samples contained small particles undetected by diffraction in the nanoparticle film that actively participate in the selenization process. This hypothesis is corroborated by a detailed investigation of the particles comprising the nanoparticle ink after size separation,[12] which reveals that the nanoparticle inks in question consist of particles from two populations with different size-correlated compositions: Cu- and Sn-rich particles roughly 5 nm in diameter and Zn-rich particles 10 to 20 nm in diameter (herein referred to as “small” and “large” particles, respectively). The study also shows that nanoparticle films containing a roughly 1:1 mixture by mass of the small and large particles create a more homogeneous, pure-phase CZTSSe film upon selenization and lead to higher

[a] School of Chemical Engineering, Purdue University, West Lafayette, IN 47906, USA. E-mail: agrawalr@purdue.edu
[b] Helmholtz-Zentrum Berlin für Materialien und Energie, Hahn-Meitner-Platz 1, 14109 Berlin, Germany.
[c] School of Materials Engineering, Purdue University, West Lafayette, IN 47906, USA.
[d] Center for Functional Nanomaterials, Brookhaven National Laboratory, Upton, NY 11973, USA.

† Electronic Supplementary Information (ESI) available: EDXRD peak assignments, full-range EDXRD data, cross-section SEM-EDS compositional maps. See DOI: 10.1039/x0xx00000x

solar cell efficiencies compared to films of the small and large particles individually.[12] Incidentally, the overall slightly Cu-poor and Zn-rich composition of the mixed particles corresponds to the composition that both theory and empirical experimentation have established as optimal for defect formation in the CZTSSe film and, consequently, its function as a photovoltaic absorber layer.[3,14,15] Thus, the mixed particle cation composition represents the target composition for processed CZTSSe absorbers. Table 1 presents the relative cation ratios determined from scanning electron microscope (SEM) energy-dispersive x-ray spectroscopy (EDS) measurements for the large, mixed, and small nanoparticle populations prepared according to the recipe described in Ref. 12. It should be noted that due to the technique used to size-separate the particles, some small particles exist in the sample of large particles, but the samples of separated small particles are free of large particles.

**Table 1** Cation ratios calculated via EDS compositional analysis for large, mixed, and small particles.[12]

| Cation Ratio | Large | Mixed | Small |
|---|---|---|---|
| Cu/(Zn+Sn) [avg. ± std. dev.]‡ | 0.64 ± 0.03 | 0.74 ± 0.02 | 1.06 ± 0.05 |
| Zn/Sn [avg. ± std. dev.]‡ | 1.70 ± 0.05 | 1.11 ± 0.04 | 0.37 ± 0.02 |
| Cu/Sn [avg. ± std. dev.]‡ | 1.72 ± 0.10 | 1.57 ± 0.05 | 1.46 ± 0.08 |

‡ EDS spectra were obtained from three different regions on samples from three separate particle batches, allowing the use of nine values when calculating average and standard deviation.

The EDXRD experiments conducted in Ref. 13 identified a transition through intermediate copper selenide phases during the growth of the quaternary CZTSe grains, which was proposed to be beneficial for the formation of a large grained morphology; however, the origin of the copper selenide was unclear, as its diffraction signal appeared abruptly without noticeable change in the signals from the nanoparticles in the precursor film.[13] The differences observed in the large and small particles are hypothesized to influence the various phases of growth observed in real-time EDXRD data of the unseparated (mixed) particles.

In this paper, the individual roles of the small and large particles in the selenization mechanism are studied via real-time EDXRD measurements. The results presented provide evidence that the Cu- and Sn-rich small particles are primarily responsible for the formation of the copper selenide intermediates, which in turn initiate the growth of Cu-Sn-Se grains greater in size than the so-termed large precursor particles. Subsequently, the Zn-rich large precursor particles contribute their composition to the growing grains to form a dense film of micrometer-sized CZTSSe grains.

## Experimental Methods

Nanoparticle films consisting of large, small, or mixed particles coated on Mo-coated soda-lime glass (SLG) and a ceramic crucible containing ~160 mg Se pellets are simultaneously heated in a sealed, evacuated graphite cylinder inside a stainless steel, dual-purpose rapid thermal processing (RTP) furnace and vacuum chamber. The inside of the graphite cylinder is lined with a pyrolytic layer to minimize the diffusion of Se vapor through the walls, and the bottom and top panels of the cylinder are quartz windows sealed to the cylinder with graphite gaskets and threaded fittings. A hole in the side of the cylinder is left open during evacuation of the vacuum chamber; once a base pressure of roughly $10^{-4}$ mbar is reached, a motorized plug is remotely engaged in order to seal the hole. The RTP furnace consists of eight halogen lamps, four above and four below the graphite cylinder, with a combined maximum power of 4 kW. During the real-time EDXRD measurements, a polychromatic beam of hard x-rays produced by the EDDI beamline of the BESSY II synchrotron facility is diffracted by the film inside the graphite cylinder and detected by an energy-dispersive Ge detector.[16,17] The temperature throughout the process is measured and controlled by a thermocouple positioned about 5 mm above the sample surface. Due to the heating up of the sample substrate and its consequent expansion, the alignment between the incident x-ray beam and the sample surface is maintained by controlling the vertical position of the vacuum chamber with a software feedback loop designed to maximize and preserve the fluorescence intensities in real-time throughout the process. Real-time EDXRD data are obtained during the selenization process using two different temperature ramp profiles – a “fast ramp” (125 K/min. from 50 °C to 500 °C, then hold 500 °C for 20 min.) and a “slow ramp” (2.9 K/min. from 200 °C to 550 °C). The slow ramp was preceded by a quicker heating to 200 °C (at ~17.5 K/min.) since no reaction is detected below this temperature. The real-time EDXRD experiment follows the work reported in Ref. 13. Further description of the nanoparticle synthesis, size-separation, and characterization is provided in Ref. 12.

## Results and Discussion

### Fast Heating

The EDXRD data in Fig. 1 show a subsection of the recorded energy and time range collected during the fast ramp selenization of large, mixed, and small particle films. Even before the heating process starts (process time 0 to 2 min.), the data show a striking difference between the three types of samples: Whereas the large and mixed particles initially show a broad peak (denoted as Σ1) near the photon energy expected for the CZTS 112 reflection (Fig. 1a,b), this peak is absent in the case of the small particles (Fig. 1c). Thus, Σ1 results exclusively from the large, Zn-rich particles. This observation can be attributed to a severe difference in the crystallinity of the large and small particles.[12]

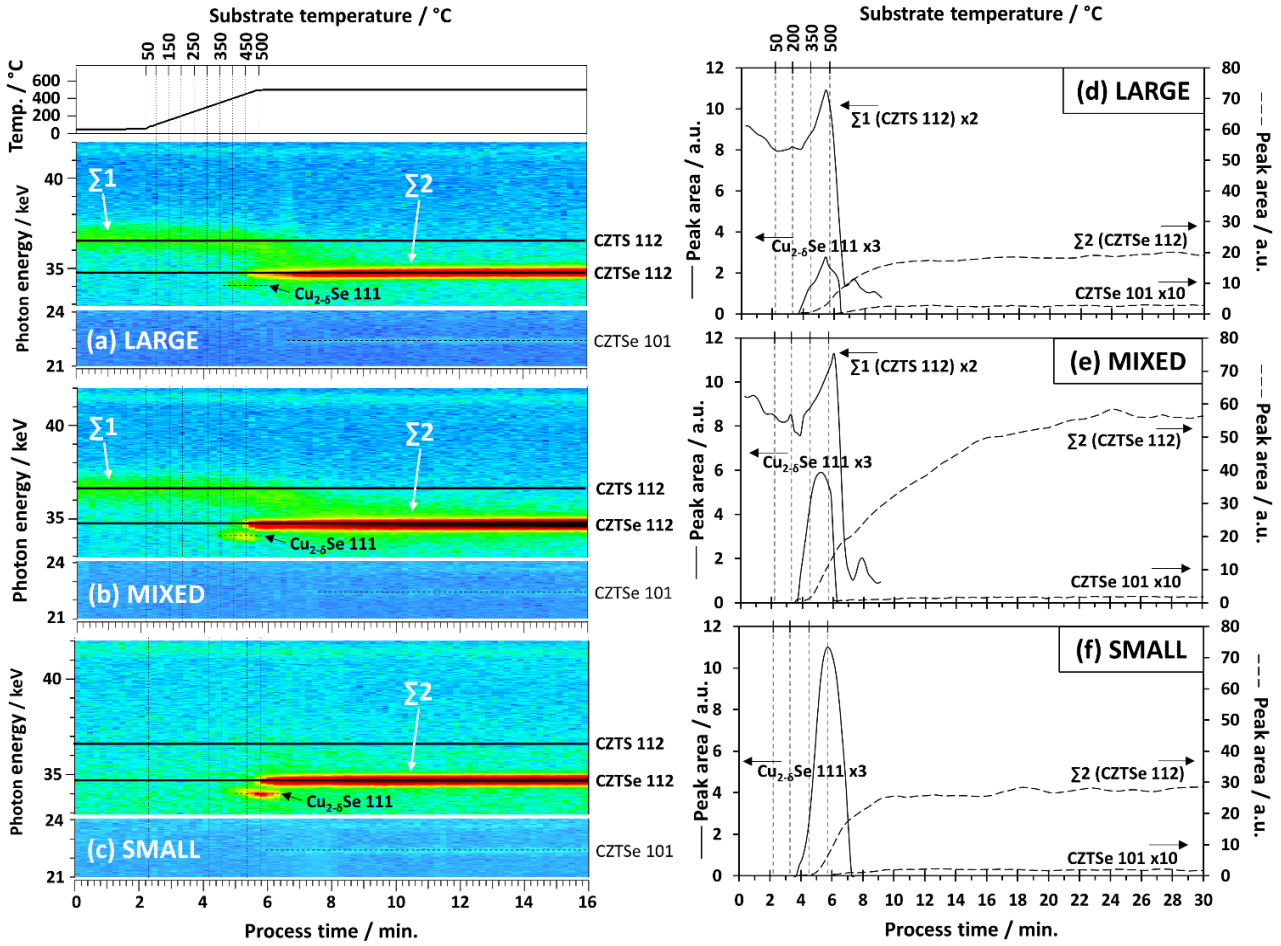


**Fig. 1** Left: Subsection of the fast ramp EDXRD data for (a) large, (b) mixed, and (c) small nanoparticle films showing the occurrence of Σ1 (at the expected position of CZTS), Σ2 (at the expected position of CZTSe), and $Cu_{2-\delta}Se$ diffraction peaks in the film. Peak assignments were made based on data from the ICDD database (CZTS: card 026-0575; CZTSe: 070-8930; $Cu_{2-\delta}Se$: 073-2712). See Supporting Information (SI) for full data range. The top part of the figure shows the temperature profile measured by a thermocouple placed roughly 5 mm above the sample surface. Right: Evolution of integrated peak intensities for fast heating of (d) large, (e) mixed, and (f) small particle films.

Despite this difference of the nanoparticles in the precursor films, the subsequent phase formation during fast heating is, at a first glance, qualitatively similar for all three precursor types: Between roughly 300 and 450 °C, additional peaks are first observed for all three samples at ~34.3 and ~34.7 keV, corresponding to $Cu_{2-\delta}Se$ 111 and the expected photon energy for the CZTSe 112 reflection, respectively. (Note that, due to the use of sulfide nanoparticle precursor films, the selenized films typically contain up to ~10% residual S compared to the total amount of S+Se; however, abbreviations for such sulfoselenide phases used hereafter generally reflect pure selenide composition for simplicity.) Due to the similar crystal structure of ZnSe and $Cu_2SnSe_3$ (CTSe) with CZTSe,[18–20] the primary peak generated near 34.7 keV is denoted as Σ2 to acknowledge the possibility that the peak could arise from any of these three phases. (The same holds for the corresponding sulfide phases and the resulting peak near 36.5 keV denoted by Σ1.[21]) However, since the peak near 22.4 keV corresponds to the 101 planes in tetragonal CZTSe,[12,13,22] we attribute Σ2 primarily to CZTSe grains once the CZTSe 101 signal is detected. During the appearance of $Cu_{2-\delta}Se$ and Σ2, the broad Σ1 peak of the large and mixed particle samples shifts towards the position of Σ2. This shift can be explained by an increase of the Se/S ratio in the large particles asymptotically to a Se concentration close to Se/(Se+S)=1.

For all three samples, the relatively brief appearance of the $Cu_{2-\delta}Se$ peak coincides with the initial growth of Σ2. However, the intensities of the $Cu_{2-\delta}Se$ signal conspicuously vary, with the small particles showing the strongest $Cu_{2-\delta}Se$ signal, the large particles the weakest, and the mixed particles an intermediate $Cu_{2-\delta}Se$ signal intensity. Qualitatively this variation of the maximum $Cu_{2-\delta}Se$ intensities correlates with the Cu/(Zn+Sn) ratio of the particles in the precursors (see Table 1). However, a comparison of the quantitative $Cu_{2-\delta}Se$ integrated intensities with the integral Cu amount in the precursors shows that the differences in the Cu content alone cannot explain the strong differences in the $Cu_{2-\delta}Se$ peak intensities; the maximum $Cu_{2-\delta}Se$ integrated intensities for large:mixed:small precursor films (Fig. 1d-f) are ~1:3:5 while the integral Cu amounts in the precursors are 1.0:1:12:1:05.[§] In other words, $Cu_{2-\delta}Se$ formation is suppressed with increasing presence of Zn in the film despite an overall similar

amount of Cu present. Moreover, in all three samples, $Cu_{2-\delta}Se$ forms rather than CTSe despite an overall Cu-poor composition with regard to Sn (i.e. Cu/Sn < 2, see Table 1); independent from the Zn/Sn ratio, in thermodynamic equilibrium Cu-Se formation would only be expected if Cu/Sn > 2.[23,24] Despite an initial Cu-poor composition, during the selenization process the composition could, in principle, exceed Cu/Sn > 2 due to loss of Sn in the form of SnS or SnSe.[25,26] However, in such a case, $Cu_{2-\delta}Se$ would be expected to be detected throughout the remainder of the process, since insufficient Sn would be available to fully convert $Cu_{2-\delta}Se$ into CZTSe or CTSe.

We conclude that kinetic mechanisms are responsible for the $Cu_{2-\delta}Se$ formation and that they are strongly influenced by the presence of the small particles. In our proposed mechanism, the small particles break down or melt during heating due to their off-target stoichiometry and diminutive size (resulting in a high surface energy).[27] The Se at the film surface quickly reacts with the loosely bound Cu to form $Cu_{2-\delta}Se$; it should be noted here that a high reactivity of Cu with Se could serve as an additional contributing factor to the disintegration of small particles. The reaction of Cu with Se at the film surface incurs a Cu chemical potential gradient in the film, driving Cu diffusion toward the surface; indeed, we have previously found a Cu enrichment of the surface shortly after the presence of $Cu_{2-\delta}Se$.[13] In contrast to a reaction within the bulk of the nanoparticle film, grains at the surface have enough space to grow to large sizes, which is energetically preferred due to lower surface energies. The growth of Cu-Se intermediates at the film surface has similarly been observed during the formation of CZTSSe[28] and CIGSe[29] absorber films

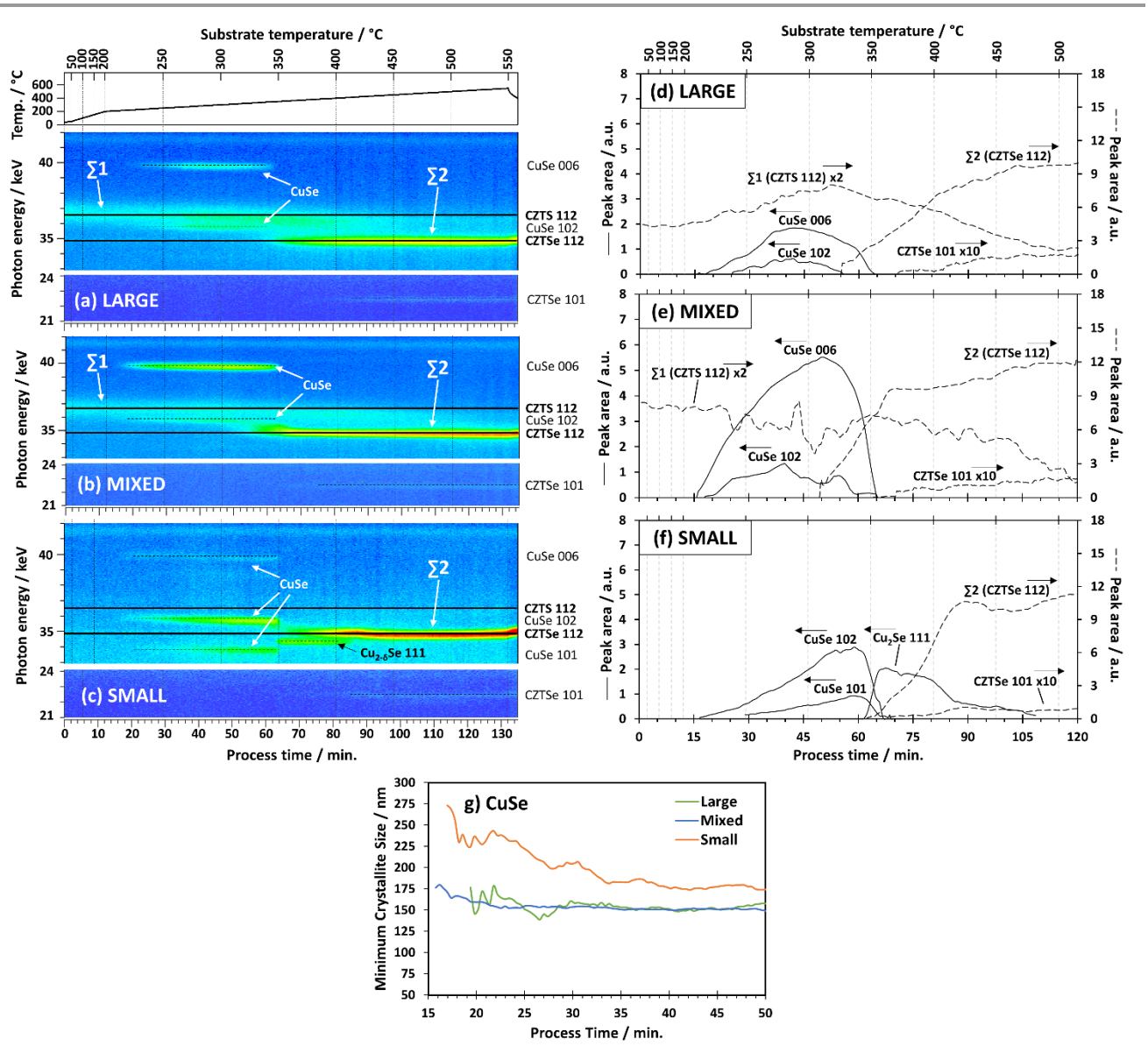


Fig. 2 Left: Subsection of the slow ramp EDXRD data for (a) large, (b) mixed, and (c) small particle films showing the occurrence of Σ1, Σ2, CuSe, and Cu2-δSe diffraction peaks in the film. Peak assignments for CuSe were made based on ICDD card 086-1240). See SI for full data range. Right: Evolution of integrated peak intensities for slow heating of (d) large, (e) mixed, and (f) small particle films. Bottom: (g) Minimum crystallite size (D/k) as described in Ref. 13 estimated using the most intense peak in each sample for CuSe (i.e. 006 planes for large and mixed particle films, 102 planes for small precursor film) during slow heating.

from metallic precursors. In these cases and others,[13,30–32] the presence or formation of Cu-Se grains has been proposed to enhance the growth of large-grain CZTSSe and CIGSe, and investigations into the synthesis mechanism of CZTS and $CuIn(S,Se)_2$ (CISSe) nanoparticles in solution have reported copper sulfide or selenide intermediates as seed phases from which CZTS and CISSe grow.[33–38] These phenomena have been attributed to a high reactivity of Cu with chalcogen (compared to Sn and Zn with chalcogen) as well as a high mobility of Cu ions, which enables Cu to easily diffuse to the reaction front, and thus are in good agreement with our proposed mechanism. The observation from Fig. 1 that $Cu_{2-\delta}Se$ formation correlates with the amount of small particles in the nanoparticle film indicates that the release of Cu from the small particles plays a crucial role in the intermediate $Cu_{2-\delta}Se$ formation.

**Slow Heating**

While the fast heating process mimics the selenization conditions used during the standard absorber formation process in device fabrication,[7–9,12] the rapid dynamics of the reaction under these conditions obscure subtle but informative details of the selenization mechanism. Thus, EDXRD data were recorded during slow heating for the large, mixed, and small particle films (Fig. 2) in order to investigate the selenization mechanism in more detail, with special attention to the correlation between the copper selenide intermediates and the evolution of Σ2 – and ultimately the formation of CZTSSe.

During slow heating, peaks corresponding to the 102 and 006 planes in hexagonal CuSe[39,40] are observed for all three samples between ~225 and ~350 °C. A third peak attributed to the 101 planes in hexagonal CuSe is observed when slow heating the small particle sample within the same temperature range (Fig. 2c). Note that the observation of CuSe peaks in all three samples contrasts with the inference of $Cu_{2-\delta}Se$ formed during fast heating. In Fig. 2a-f, the relative intensity of the CuSe peaks from the 102 and 006 crystal planes is different for the small particle sample than for the large and mixed precursor films, indicating the CuSe grains grow with a preferred texture in the absence of the large, Zn-rich particles based on the expected relative peak intensities for hexagonal CuSe.[39,40] In the small particle sample, CuSe quickly vanishes near 350 °C while a strong $Cu_{2-\delta}Se$ signal appears (Fig. 2c), suggesting CuSe undergoes a transition to $Cu_{2-\delta}Se$ wherein Cu is reduced and Se is liberated from the crystal lattice; this transition has similarly been observed for co-evaporated Cu-Se films (albeit at a slightly higher temperature of 377 °C), in which the liberated Se manifests as a liquid phase.[40] Markedly, the first appearance of Σ2 in the small particle film coincides with this copper selenide phase transition. It is also worthwhile to note the transition from CuSe to $Cu_{2-\delta}Se$ is not observed in the mixed or large particle films (Fig. 2a,b). Instead, in these cases Σ2 forms at lower temperatures (around 320 °C; see Fig. 2d,e) during the decrease of the CuSe signal. The absence of CuSe in the fast ramp EDXRD data may be attributable to the temperature ramp rate: By the time a

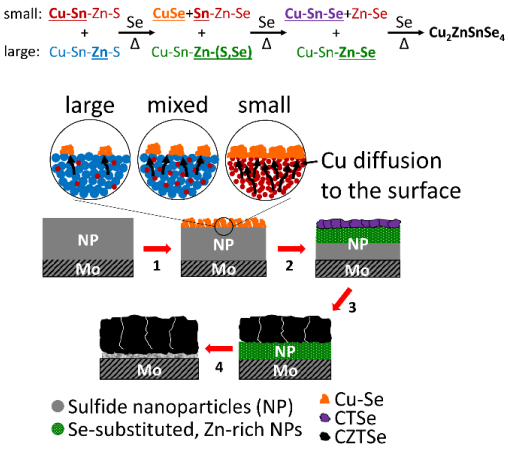


**Fig. 3** Schematic process pathway (top) and diagram (bottom) of the proposed selenization pathway accounting for the roles of interparticle heterogeneities. In the schematic process pathway, the bold and underlined elements represent those which represent the majority alloy consitutent(s) for the small and large nanocrystals (along the top and bottom rows of the pathway, respectively) and their resultant phases throughout the process. Note that "Sn-Zn-Se" refers to coexisting selenides of Sn and Zn rather than a ternary $Sn_xZn_ySe_z$ phase, since no such compound is known to be stable. Additionally, the phases in the process pathway are color-coded with their corresponding phases in the diagram – red: small, sulfide nanocrystal precursors; blue: large, sulfide nanocrystal precursors; orange: Cu-Se grains that initially form at the top of the film surface; green: selenized large precursor grains; purple: Cu-Sn-Se grains that result from Sn incorporating into Cu-Se; and black: micrometer-sized CZTSe grains.

detectable amount of copper selenide forms, the temperature has surpassed the threshold at 350 °C where CuSe converts to $Cu_{2-\delta}Se$. The suppression of CuSe formation in the fast heating process can also be supported by a delay of Se evaporation due to slower Se heating relative to substrate heating.

The slow heating EDXRD data show that the CuSe peaks occurring during selenization of the small particle sample exhibit reduced peak broadening compared to the large and mixed particle samples. The minimum average crystallite size calculated from the peak broadening reaches values above 200 nm for the small particle precursor film, while that for the large and mixed precursor films ranges between 150 and 175 nm throughout the process (Fig. 2g). This observation supports the assertion that the presence of the small particles in the precursor film enhances the growth of large Cu-Se grains.

**Role of Interparticle Heterogeneities in the Selenization Pathway**

The EDXRD data presented in Figs. 1 and 2 lead to three key observations regarding the roles of the interparticle heterogeneities during the selenization process:

First, since Σ1 is not observed for the small particle sample Fig. 1c,f, 2c,f), any behavior of this signal corresponds to phenomena solely affecting the large, Zn-rich particles. Thus, the gradual shift of Σ1 from the CZTS 112 position early in the process to the CZTSe 112 position by the end of the process indicates the substitution of S with Se in the large particles.

Second, the positive correlation between the signal intensities from copper selenide intermediates and the proportion of small particles in each sample – particularly during fast heating (Fig. 1d-f) – suggests that the copper

selenide formation primarily results from the small particles. Since the small particles contain the majority of the Cu content in the samples, it follows that formation of Cu-containing intermediates could be primarily attributed to the release of Cu from these particles. However, even if both the large and small particles comprised similar composition near the target for CZTSSe absorbers, the high surface energy of the small particles due to their size would be expected to result in relative instability of these particles compared to their larger counterparts, which in turn might cause the smaller particles to more readily release Cu for its reaction with Se.

The third key observation from the real-time EDXRD measurements is the concurrence of the initial detection of Σ2 with the behavior in the signals from the copper selenide intermediates. For the small particles during slow heating, the rise of Σ2 coincides with the CuSe-to-$Cu_{2-\delta}Se$ transition (Fig 2f), while in all other cases (Fig. 1d-f, 2d,e) the rise of Σ2 coincides with a fast drop in signal intensity of Cu-Se. This observation suggests the copper selenide intermediates contribute to the nucleation and early growth of the phase generating Σ2, which ultimately becomes the desired CZTSSe. Furthermore, the initial growth rate of Σ2 for the small and mixed particle films, which show higher Cu-Se signal intensities, is greater than that in the large particle samples independent of the heating rate. Thus, the presence of small particles and/or the copper selenide intermediates seem to facilitate the growth of the phase generating Σ2, namely CTSe or CZTSe. For the cases of slow heating large and mixed particle films, CuSe is consumed for the formation of Σ2 before the temperature of the CuSe to $Cu_{2-\delta}Se$ transition is reached, since the early appearance of Σ2 coincides with the decline in the CuSe signal (Fig. 2d,e). We propose that the CuSe grains in the large and mixed films react with Sn at a temperature lower than the CuSe-to-$Cu_{2-\delta}Se$ transition – potentially due to their smaller size in these films compared to the small particle film – resulting in the earlier formation of Σ2 compared to the small particle film.

These observations provide details which allow modification of the mixed-particle selenization pathway proposed in Ref. 13 to account for the roles of the interparticle heterogeneities characterized in Ref. 12. Each of the following steps in the pathway corresponds to the commonly numbered step depicted in Fig. 3:

1. Growth of Cu-Se grains at the top surface of the film via release and diffusion of Cu from small particles and its reaction with Se.
2. Reaction of residual Sn from small particles with Cu-Se to form CTSe; concurrently, substitution of S with Se in large, Zn-rich particles.
3. Reaction of CTSe with selenized Zn-rich grains to form CZTSe, and progression of CZTSe grain growth downward through the film.
4. Given the proper overall film composition (i.e. near-target) and sufficient cation diffusion, the complete incorporation of cations into a relatively homogeneous film comprising quaternary CZTSe grains.

## Conclusions

Real-time EDXRD analysis has been utilized to investigate the selenization mechanism of three Cu-Zn-Sn-S nanoparticle populations: large particles 10-20 nm in size exhibiting a Zn-rich composition, small particles ~5 nm in diameter that are rich in Cu and Sn, and a roughly 1:1 mixture by mass of the large and small particles that manifests a slightly Cu-poor and Zn-rich composition compared to the $Cu_2ZnSnS_4$ stoichiometry. Upon selenization, the small, Cu- and Sn-rich nanoparticles lead to the formation of copper selenide intermediates, which in turn initiate the growth of grains that ultimately become the desired quaternary CZTSe. We therefore conclude that including the small particles in the nanoparticle precursor film strongly influences the selenization mechanism and, in turn, CZTSe absorber formation. While the large particles do not appear to contribute to the formation of copper selenide, they support the growth of CZTSe grains as a cation source over time. These results help clarify and expand upon our previous finding that including the small particles in the nanoparticle films prior to selenization leads to improved solar cell efficiencies for two different nanoparticle synthesis recipes, notably even when the large particles exhibit a slightly Cu-poor, Zn-rich composition close to the target.[12] Providing a pathway for forming dense, phase-pure films of large grains, the details of the CZTSSe grain growth mechanism presented herein greatly benefit ongoing efforts to improve the quality of CZTSSe absorbers and solar cell efficiencies.

## Acknowledgements

Special thanks go to Jakob Lauche and Guido Wagener for their support during the real-time measurements at BESSY II, and to Kevin Brew for preparing the Mo-coated SLG substrates. This work was funded by the NSF Solar Economy IGERT (award #DGE-0903670). The funding of OZ by the German Ministry of Education and Research within the project PINET (03SF0358F) is gratefully acknowledged. EAS acknowledges support to the Center for Functional Nanomaterials, Brookhaven National Laboratory, which is supported by the U.S. Department of Energy, Office of Basic Energy Sciences, under Contract No. DE-SC0012704.

## Notes and References

§ Here, the integral Cu amount for each sample is determined by multiplying the Cu/Sn ratio in Table 1 with the integrated intensity of the Sn-Kα fluorescence signal near 25 keV in the fast ramp EDXRD spectra at the beginning of the process: 5.74, 7.35, and 7.09 (in arbitrary units) for the large, mixed, and small samples, respectively.

1 D. B. Mitzi, O. Gunawan, T. K. Todorov, K. Wang and S. Guha, *Sol. Energy Mater. Sol. Cells*, 2011, **95**, 1421–1436.
2 A. Redinger, D. M. Berg, P. J. Dale, R. Djemour, G. Levent, T. Eisenbarth, N. Valle and S. Siebentritt, *IEEE J. Photovoltaics*, 2011, **1**, 200–206.
3 W. Wang, M. T. Winkler, O. Gunawan, T. Gokmen, T. K. Todorov, Y. Zhu and D. B. Mitzi, *Adv. Energy Mater.*, 2013.

 

4 Y. S. Lee, T. Gershon, O. Gunawan, T. K. Todorov, T. Gokmen, Y. Virgus and S. Guha, *Adv. Energy Mater.*, 2015, **5**, 1401372.
5 I. Repins, C. Beall, N. Vora, C. Dehart, D. Kuciauskas, P. Dippo, B. To, J. Mann, W. Hsu, A. Goodrich and R. Noufi, *Sol. Energy Mater. Sol. Cells*, 2012, **101**, 154–159.
6 G. Brammertz, M. Buffière, S. Oueslati, H. ElAnzeery, K. Ben Messaoud, S. Sahayaraj, C. Köble, M. Meuris and J. Poortmans, *Appl. Phys. Lett.*, 2013, **103**, 163904.
7 C. K. Miskin, W. C. Yang, C. J. Hages, N. J. Carter, C. S. Joglekar, E. A. Stach and R. Agrawal, *Prog. Photovoltaics Res. Appl.*, 2015, **23**, 654–659.
8 C. J. Hages, S. Levcenco, C. K. Miskin, J. H. Alsmeier, D. Abou-Ras, R. G. Wilks, M. Bär, T. Unold and R. Agrawal, *Prog. Photovoltaics Res. Appl.*, 2013, **23**, 376–384.
9 Q. Guo, G. G. M. Ford, W.-C. W. Yang, B. C. Walker, E. A. Stach, H. W. Hillhouse and R. Agrawal, *J. Am. Chem. Soc.*, 2010, **132**, 17384–17386.
10 Q. Guo, G. M. Ford, H. W. Hillhouse and R. Agrawal, *Nano Lett.*, 2009, **9**, 3060–3065.
11 C. K. Miskin, N. J. Carter, W. Yang, C. J. Hages, E. Stach and R. Agrawal, in *Proceedings of the 39th IEEE Photovoltaics Specialists Conference*, Tampa, FL, USA, 2013, vol. 1, pp. 0034 – 0037.
12 N. J. Carter, W. Yang, C. K. Miskin, C. J. Hages, E. A. Stach and R. Agrawal, *Sol. Energy Mater. Sol. Cells*, 2014, **123**, 189–196.
13 R. Mainz, B. C. Walker, S. S. Schmidt, O. Zander, A. Weber, H. Rodriguez-Alvarez, J. Just, M. Klaus, R. Agrawal and T. Unold, *Phys. Chem. Chem. Phys.*, 2013, **15**, 18281–18289.
14 S. Chen, J.-H. Yang, X. G. Gong, A. Walsh and S.-H. Wei, *Phys. Rev. B*, 2010, **81**, 245204.
15 K. Tanaka, Y. Fukui, N. Moritake and H. Uchiki, *Sol. Energy Mater. Sol. Cells*, 2011, **95**, 838–842.
16 H. Rodriguez-Alvarez, I. M. Kötschau and H. W. Schock, *J. Cryst. Growth*, 2008, **310**, 3638–3644.
17 C. Genzel, I. a. Denks, R. Coelho, D. Thomas, R. Mainz, D. Apel and M. Klaus, *J. Strain Anal. Eng. Des.*, 2011, **46**, 615–625.
18 H. F. McMurdie, M. C. Morris, E. H. Evans, B. Paretzkin, W. Wong-Ng and C. R. Hubbard, *Powder Diffr.*, 2013, **1**, 265–275.
19 B. B. Sharma, R. Ayyar and H. Singh, *Phys. Status Solidi*, 1977, **40**, 691–696.
20 G. E. Delgado, a. J. Mora, G. Marcano and C. Rincón, *Mater. Res. Bull.*, 2003, **38**, 1949–1955.
21 P. A. Fernandes, P. M. P. Salomé and A. F. da Cunha, *J. Alloys Compd.*, 2011, **509**, 7600–7606.
22 M. Brandl, R. Ahmad, M. Distaso, H. Azimi, Y. Hou, W. Peukert, C. J. Brabec and R. Hock, *Thin Solid Films*, 2015, **582**, 269–271.
23 I. D. Olekseyuk, I. V. Dudchak and L. V. Piskach, *J. Alloys Compd.*, 2004, **368**, 135–143.
24 I. V. Dudchak and L. V. Piskach, *J. Alloys Compd.*, 2003, **351**, 145–150.
25 A. Redinger, D. M. Berg, P. J. Dale and S. Siebentritt, *J. Am. Chem. Soc.*, 2011, **133**, 3320–3323.
26 A. Weber, R. Mainz and H. W. Schock, *J. Appl. Phys.*, 2010, **107**, 013516.
27 S. Lai, J. Guo, V. Petrova, G. Ramanath and L. Allen, *Phys. Rev. Lett.*, 1996, **77**, 99–102.
28 C. M. Fella, A. R. Uhl, C. Hammond, I. Hermans, Y. E. Romanyuk and A. N. Tiwari, *J. Alloys Compd.*, 2013, **567**, 102–106.
29 R. Mainz, A. Weber, H. Rodriguez-Alvarez, S. Levcenko, M. Klaus, P. Pistor, R. Klenk and H. Schock, *Prog. Photovoltaics Res. Appl.*, 2014, Available online. DOI: 10.1002/pip.2531
30 R. Klenk, T. Walter, H.-W. Schock and D. Cahen, *Adv. Mater.*, 1993, **5**, 114–119.
31 W. K. Kim, E. a. Payzant, T. J. Anderson and O. D. Crisalle, *Thin Solid Films*, 2007, **515**, 5837–5842.
32 B. C. Walker and R. Agrawal, in *2012 38th IEEE Photovoltaic Specialists Conference*, IEEE, 2012, pp. 002654–002657.
33 M. D. Regulacio, C. Ye, S. H. Lim, M. Bosman, E. Ye, S. Chen, Q.-H. Xu and M.-Y. Han, *Chemistry*, 2012, **18**, 3127–3131.
34 S. T. Connor, C.-M. Hsu, B. D. Weil, S. Aloni and Y. Cui, *J. Am. Chem. Soc.*, 2009, **131**, 4962–4966.
35 M. Kruszynska, H. Borchert, J. Parisi and J. Kolny-Olesiak, *J. Am. Chem. Soc.*, 2010, **132**, 15976–15986.
36 Q. Guo, S. J. Kim, M. Kar, W. N. Shafarman, R. W. Birkmire, E. A. Stach, R. Agrawal and H. W. Hillhouse, *Nano Lett.*, 2008, **8**, 2982–7.
37 M. Kar, R. Agrawal and H. W. Hillhouse, *J. Am. Chem. Soc.*, 2011, **133**, 17239–17247.
38 A. D. Collord and H. W. Hillhouse, *Chem. Mater.*, 2015, **27**, 1855–1862.
39 H. Nozaki, K. Shibata, M. Onoda, K. Yukino and M. Ishii, *Mater. Res. Bull.*, 1994, **29**, 203–211.
40 J. O. Thompson, M. D. Anderson, T. Ngai, T. Allen and D. C. Johnson, *J. Alloys Compd.*, 2011, **509**, 9631–9637.